JACS
JOURNAL OF THE AMERICAN CHEMICAL SOCIETY
Communication
pubs.acs.org/JACS

Structurally Tailored Hexagonal Ferroelectricity and Multiferroism in Epitaxial $YbFeO_3$ Thin-Film Heterostructures

Young Kyu Jeong,[†,‡] Jung-Hoon Lee,[†,‡] Suk-Jin Ahn,[†] Seung-Woo Song,[†] Hyun Myung Jang,*[,†,§] Hyojin Choi,[∥] and James F. Scott[⊥]

[†]Department of Materials Science and Engineering and Division of Advanced Materials Science, and [§]Department of Physics, Pohang University of Science and Technology (POSTECH), Pohang 790-784, Republic of Korea

[∥]Department of Beamline, Pohang Accelerator Laboratory (PAL), Pohang 790-784, Republic of Korea

[⊥]Cavendish Laboratory, Department of Physics, University of Cambridge, Cambridge CB3 0HE, United Kingdom

Supporting Information

ABSTRACT: Multiferroics have received a great deal of attention because of their fascinating physics of order-parameter cross-couplings and their potential for enabling new device paradigms. Considering the rareness of multiferroic materials, we have been exploring the possibility of artificially imposing ferroelectricity by structurally tailoring antiferromagnets in thin-film forms. $YbFeO_3$ (YbFO hereafter), a family of centrosymmetric rare-earth orthoferrites, is known to be nonferroelectric (space group *Pnma*). Here we report that a YbFO thin-film heterostructure fabricated by adopting a hexagonal template surprisingly exhibits nonferroelastic ferroelectricity with the Curie temperature of 470 K. The observed ferroelectricity is further characterized by an extraordinary two-step polarization decay, accompanied by a pronounced magnetocapacitance effect near the lower decay temperature, ∼225 K. According to first-principles calculations, the hexagonal $P6_3/mmc$–$P6_3mc$–$P6_3cm$ consecutive transitions are primarily responsible for the observed two-step polarization decay, and the ferroelectricity originates from the *c*-axis-oriented asymmetric Yb $5d_{z^2}$–O $2p_z$ orbital hybridization. Temperature-dependent magnetization curves further reveal an interesting phenomenon of spontaneous magnetization reversal at 83 K, which is attributed to the competition between two distinct magnetocrystalline anisotropy terms, Fe 3d and Yb 4f moments.

Over the past decade, there has been a resurgence of interest in understanding and applications of multiferroic materials.[1−10] Among numerous multiferroics currently under investigation, rare-earth manganites have been most extensively studied owing to their tendency toward strong magnetoelectric (ME) coupling, in general. They are classified into two distinct crystal classes depending on the radius of rare-earth cation. $ReMnO_3$-type oxides with Re = La−Dy in the lanthanide series belong to orthorhombic manganites,[2,6,8] while $ReMnO_3$-type oxides with Re = Ho−Lu belong to hexagonal manganites.[10−13] Unlike orthomanganites, hexagonal manganites possess *c*-axis-oriented ferroelectricity owing to the disappearance of a mirror image on the *a*−*b* plane with a tilting of the MnO_5 bipyramid units.[12−14] They also exhibit an antiferromagnetic (AFM) order below the magnetic ordering temperature, as Mn^{3+} spins are oriented parallel to the *a*−*b* plane with a so-called 120° triangular spin structure.[13−16]

Contrary to the two distinct structural polymorphs observed in rare-earth manganites, all of the $ReFeO_3$-type oxides belong to orthorhombic ferrites (orthoferrites) and are characterized by corner-linked FeO_6 octahedra forming a three-dimensional network in a centrosymmetric *Pnma* (or *Pbnm*) unit cell.[17,18] Accordingly, all of the rare-earth orthoferrites are known to be non-ferroelectric at room temperature except for the recently reported improper ferroelectricity in $SmFeO_3$, which is caused by the canted AFM spin ordering through a reverse Dzyaloshinskii−Moriya interaction.[19] Considering the *c*-axis-oriented structural ferroelectricity observed in hexagonal manganites, we have been exploring the possibility of artificially imposing ferroelectricity and thus multiferroism by structurally tailoring an AFM orthoferrite, $ReFeO_3$, in a constrained thin-film form. Indeed, Bossak and co-workers[20] reported the fabrication of epitaxially stabilized hexagonal orthoferrite $ReFeO_3$ (Re = Eu−Lu) thin films on ZrO_2 (Y_2O_3) substrates. However, their study was limited to structural characterizations. Thus, it is of great scientific importance to clearly elucidate the nature of ferroelectricity in hexagonal ferrites, if any, and to identify the possible variation of magnetic responses arising from the orthorhombic-to-hexagonal transformation.

In this study, we will demonstrate artificially imposed hexagonal ferroelectricity using a $YbFeO_3$ (YbFO hereafter) thin film heteroepitaxially grown on a hexagonal substrate, Pt (111)/sapphire. Interestingly, the observed ferroelectricity is characterized by an extraordinary two-step polarization decay, accompanied by a pronounced magnetocapacitance effect in the vicinity of the lower decay temperature, ∼225 K. On the basis of first-principles calculations, we attribute the hexagonal ferroelectricity to asymmetric Yb $5d_{z^2}$–O $2p_z$ orbital hybridization.

The θ–2θ X-ray diffraction patterns indicate that the YbFO film grown on a Pt(111)/sapphire (0001) substrate by pulsed laser deposition is highly *c*-axis oriented. Both Φ-scan spectra and pole figures further reveal that the YbFO film (thickness of

Received: November 3, 2011
Published: January 10, 2012

   dx.doi.org/10.1021/ja210341b | J. Am. Chem.Soc. 2012, 134, 1450−1453

~60 nm) is not orthorhombic but is grown epitaxially with six-fold hexagonal symmetry [Figure S1 in the Supporting Information (SI)]. Accordingly, the YbFO film is expected to exhibit ferroelectricity along the *c*-axis of a noncentrosymmetric hexagonal cell. As presented in Figure 1a, the polarization–

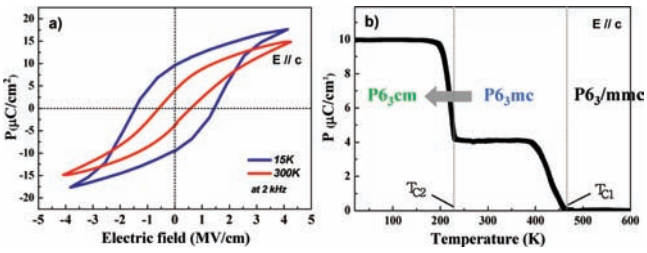

Figure 1. (a) Polarization–field (P–E) hysteresis loops obtained at 15 and 300 K. The 60-nm-thick $YbFeO_3$ thin film used in the P–E hysteresis measurement was heteroepitaxially grown on a Pt(111)/sapphire (0001) substrate. (b) Temperature-dependent spontaneous polarization curve of the epitaxial $YbFeO_3$ thin film, showing a characteristic two-step polarization decay.

electric field (P–E) curves demonstrate that the hexagonal $YbFeO_3$ (h-YbFO) thin film is ferroelectric at room temperature. Both the remanent polarizarion (P_r) and the squareness in the P–E curve are enhanced with decreasing temperature: from P_r = 4.0 μC/cm^2 at 300 K to 10.0 μC/cm^2 at 15 K. The spontaneous polarization (P_s) was determined by measuring the temperature-dependent pyroelectric current and subsequently integrating this current as a function of temperature (Figure S3). Interestingly, the temperature-dependent P_s is characterized by an extraordinary two-step polarization decay (Figure 1b). From this curve, one can clearly conclude that the ferroelectric Curie temperature is ~470 K (T_{c1}) and the onset of the second ferroelectric transition (T_{c2}) is ~225 K.

We then examined a possible phase-transition path that would lead to this extraordinary two-step polarization decay. According to group theoretical analysis,[21,22] we have three possible transition paths that connect the high-temperature paraelectric $P6_3/mmc$ phase to the ground-state $P6_3cm$ phase. The first allowed path denotes a phase transition sequence of $P6_3/mmc$–$P6_3mc$–$P6_3cm$ with decreasing temperature. Thus, this path involves an intermediate ferroelectric phase, $P6_3mc$. On the other hand, the second possible transition route involves an intermediate paraelectric phase of $P6_3/mcm$ with the unit-cell tripling. In this case, a phase transition sequence of $P6_3/mmc$–$P6_3/mcm$–$P6_3cm$ is expected. The third possible path refers to a direct transition to the ferroelectric ground state, i.e., $P6_3/mmc$–$P6_3cm$. Thus, among the three possible paths that satisfy a group–subgroup relation, only the first path involves an intermediate ferroelectric phase. In this case, one would expect a two-step polarization decay caused by the $P6_3/mmc$–$P6_3mc$ transition at T_{c1} and the $P6_3mc$–$P6_3cm$ transition at T_{c2}. This sequential mechanism satisfactorily accounts for the observed stepwise polarization decay (Figure 1b). It is interesting to note that the constrained h-YbFO is non-ferroelastic since the $P6_3/mmc$–$P6_3mc$–$P6_3cm$ phase transitions do not induce any change in the crystal class.[23]

Having resolved the phase-transition path responsible for the two-step polarization decay, we have then examined (i) variations of the crystal structure associated with these sequential transitions and (ii) the electronic origin of the ferroelectricity by performing density-functional theory (DFT) calculations. In the paraelectric $P6_3/mmc$ phase, all the ions are confined to the planes that are parallel to the a–b plane, with the mirror plane perpendicular to the *c*-axis (marked in blue in Figure 2a). On the other hand, upon the transition to $P6_3mc$,

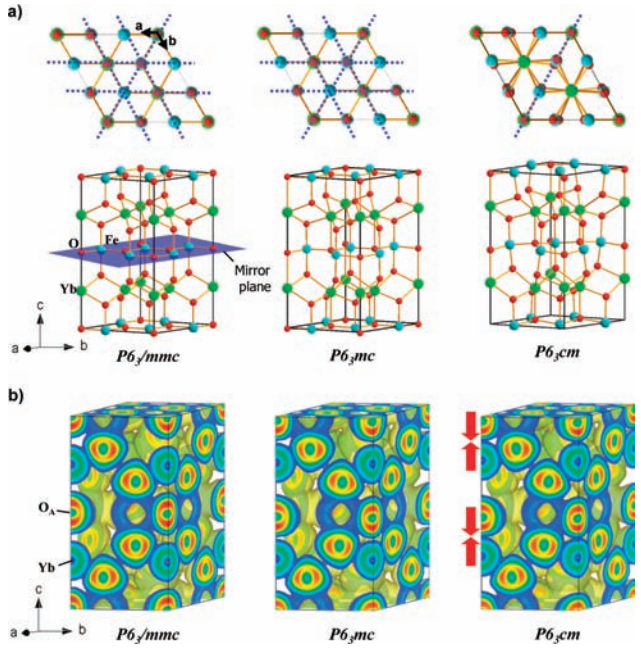

Figure 2. (a) Computed crystal structures of $P6_3/mmc$, $P6_3mc$, and $P6_3cm$ phases. The two-dimensionally projected structure on the hexagonal a–b plane is shown in the upper panel, where the dotted blue lines denote the mirror-plane symmetry parallel to the *c*-axis. On the other hand, three-dimensional crystal structures are compared in the lower panel. (b) The three-dimensional electron-density contour of the paraelectric $P6_3/mmc$ phase is compared with those of the two ferroelectric phases, $P6_3mc$ and $P6_3cm$.

this mirror plane disappears while the mirror planes parallel to the *c*-axis remain invariant. Consequently, the *c*-axis-oriented ferroelectricity appears in the $P6_3mc$ phase. The transition to the ferroelectric ground state of $P6_3cm$ follows, with an additional tilting of the FeO_5 bipyramid cages. Consequently, all the in-plane and out-of-plane mirror images except for $[110]_h$ disappear in the $P6_3cm$ phase. The DFT polarizations obtained using the Berry phase method[24] are 4.0 μC/cm^2 for the $P6_3mc$ phase and 10.5 μC/cm^2 for the $P6_3cm$ phase. These values agree well with the experimentally obtained values (Figure 1b).

Let us now examine the bonding nature of the hexagonal ferroelectricity. For this purpose, we first compare the computed electron localization function (ELF) of the paraelectric $P6_3/mmc$ phase with those of the two ferroelectric phases, since the ELF (i.e., electron density contour) is known to be an informative tool to distinguish different bonding interactions in solids.[14,25] As shown in Figure 2b, the electron density between the Yb ion and the axial oxygen (O_A) is negligible for both $P6_3/mmc$ and $P6_3mc$ phases, which demonstrates a dominant ionic bonding character in the Yb–O_A bond. Upon the transition to the $P6_3cm$ ground state, however, there occurs a strong asymmetric covalent bonding interaction between the Yb ion and one of the two O_A ions along the *c*-axis (marked with red arrows in Figure 2b). This asymmetric covalent bonding is responsible for the observed large polarization of 10 μC/cm^2. Thus, one can conclude that

dx.doi.org/10.1021/ja210341b | J. Am. Chem.Soc. 2012, 134, 1450–1453

the ferroelectricity in the intermediate $P6_3mc$ phase is ionic, while the ferroelectricity in the $P6_3cm$ phase is predominantly covalent in nature.

We now address the following important point: What kinds of orbital interactions are involved in the asymmetric Yb−O_A bonding which is responsible for the *c*-axis-oriented ferroelectricity? To resolve this question, we have considered two distinct possibilities of the Yb−O_A bonding interaction: (i) empty $5d_{z^2}$(Yb)−$2p_z$(O_A) interaction and (ii) empty 6*s*(Yb)−$2p_z$(O_A) interaction. As schematically depicted in Figure 3a, the

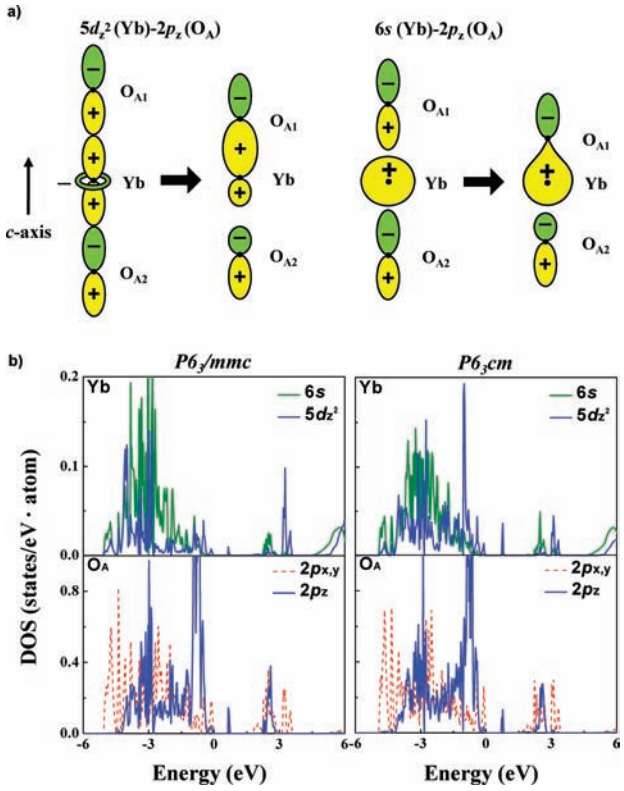

Figure 3. (a) Schematic diagrams of the two distinct possibilities of the Yb−O_A orbital interactions, $5d_{z^2}$(Yb)−$2p_z$(O_A) and 6*s*(Yb)−$2p_z$(O_A). (b) Comparison of the orbital-resolved partial density of states for $5d_{z^2}$(Yb), 6*s*(Yb), $2p_{x,y}$(O_A), and $2p_z$(O_A) orbitals of the paraelectric $P6_3/mmc$ phase with those of the ferroelectric $P6_3cm$ phase.

$5d_{z^2}$(Yb)−$2p_z$(O_A) interaction induces asymmetric covalent bonding along the *c*-axis. In this way, the central Yb ion is now able to make an asymmetric covalent bond with one of the two neighboring O_A ions (not simultaneously with two neighboring O_A ions), which results in a spontaneous breaking of the centrosymmetric state. Similarly, the 6*s*(Yb)−$2p_z$(O_A) interaction is also capable of forming asymmetric covalent bonds along the *c*-axis of $P6_3cm$ (Figure 3a). We then examined orbital-resolved partial density of states (PDOS) to elucidate the covalent bonding mechanism truly responsible for the hexagonal ferroelectricity. As shown in Figure 3b, the degree of the overlapping between the Yb 6*s* orbital PDOS and the O_A $2p_z$ orbital PDOS in the paraelectric $P6_3/mmc$ state is little changed upon the transition to the ferroelectric $P6_3cm$ state. Contrary to this, the degree of the overlapping between the Yb $5d_{z^2}$ orbital PDOS and the O_A $2p_z$ orbital PDOS is remarkably enhanced upon the transition to the $P6_3cm$ state (especially for the energy range between −1.0 and −0.3 eV below the valence-band top). Thus, the $5d_{z^2}$(Yb)−$2p_z$(O_A) hybridization is considered to be the electronic origin of the ferroelectricity.

As presented in Figure 4a, zero-field cooling (ZFC) and FC curves of the *c*-axis magnetization are separated from each other

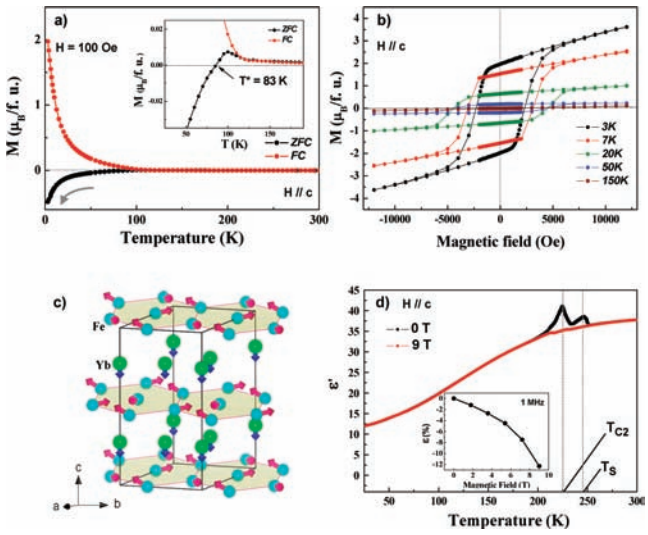

Figure 4. (a) Temperature-dependent magnetization curves (ZFC and FC) showing spontaneous magnetization reversal at *T**. (b) Magnetization−field hysteresis curves obtained at various temperatures. (c) Schematic representation of the stable ground-state spin configuration in the hexagonal $YbFeO_3$. The spins at the Yb^{3+} ion sublattice are marked with blue arrows (antiparallel to the *c*-axis), whereas the spins at the Fe^{3+} ion sublattice are denoted by red arrows. (d) Temperature-dependent relative dielectric permittivity obtained with and without applying an external magnetic field of 9 T at a measuring ac frequency of 1 MHz. (Inset) Percent change in the relative dielectric permittivity (at 1 MHz) plotted as a function of the bias magnetic field showing a pronounced magnetodielectric effect at T_{c2}.

beginning at 120 K. The onset of the ZFC−FC separation can be considered as a magnetic ordering temperature ($T_N \approx 120$ K). The *c*-axis magnetization−field (M−H) hysteresis curves measured at various temperatures show that the magnetic remanence increases while the coercive field decreases with decreasing temperature (Figure 4b). Our DFT calculations of h-YbFO predict that Fe^{3+} spins in the ground-state form a so-called 120° triangular spin structure on the *a*−*b* plane. This configuration is largely consistent with a typical spin structure for triangular AFM spins in frustrated magnetic systems such as hexagonal manganites.[13−16] Thus, one would expect a nearly zero residual moment along the in-plane direction. According to the present DFT calculations, however, Fe^{3+} spins are slightly canted with a non-zero moment along the *c*-axis, which is in contrast with a zero in-plane magnetization. The red arrows in Figure 4c denote these canted Fe^{3+} spin moments.

Upon cooling to 83 K (called a compensation temperature, *T**), h-YbFO further shows an interesting phenomenon of spontaneous magnetization reversal (Figure 4a). This suggests a long-range ordering of the Yb^{3+} moment (spin + orbital) at *T**. In this case, the direction of the net Yb^{3+} moment (−*c*) should be opposite to that of the canted Fe^{3+}-spin moment (+*c*). Our DFT calculations support this proposition and further predict that the magnitude of the orbital and spin moment of Yb^{3+} is much bigger than that of the Fe^{3+}-spin moment with the net spontaneous magnetic moment of −0.511

dx.doi.org/10.1021/ja210341b | J. Am. Chem.Soc. 2012, 134, 1450−1453

μ_B per formula unit (f.u.). This prediction is nearly consistent with the experimental value of −0.473 μ_B/f.u. at 3 K (measured under a weak field of 100 Oe). Thus, the spontaneous magnetization reversal at T^* can be attributed to the competition between two distinct magnetocrystalline anisotropy terms, namely, the ordered Yb^{3+} moment along $-c$ versus the canted Fe^{3+} spin moment along $+c$ of the $P6_3cm$ unit cell.

We have further assessed the degree of the ME coupling by examining the magnetodielectric (MD) effect of the h-YbFO film with and without applying an external magnetic field along the *c*-axis. Interestingly, the dielectric permittivity curve is characterized by two distinct dielectric anomalies in the absence of the external field (Figure 4d). Comparing these MD data with the temperature-dependent polarization curve (Figure 1b), one can readily identify that the lower dielectric anomaly point (~220 K) nearly coincides with the second ferroelectric transition temperature, T_{c2} (~225 K). As shown in the inset of Figure 4d, the MD effect is very pronounced at this temperature: about 12.3% change in the relative dielectric permittivity under a bias magnetic field of 9 T. This reflects (i) a strong biquadratic order-parameter cross-coupling between P^2 and M^2 and (ii) a magnetic-field-induced nonzero magnetization, $M(H)$, above T_N (see SI). The dielectric anomaly at T_s (~240 K) is thus not related to the rapid increase in the polarization at the onset of the $P6_3mc$–$P6_3cm$ transition (~225 K). According to the DFT calculations, the polarization change associated with the $P6_3mc$–$P6_3cm$ transition is accompanied by a large variation in the tilting degree of the FeO_5 bipyramid unit, from 0.68° (with respect to the *c*-axis) for $P6_3mc$ to 6.32° for $P6_3cm$. Thus, the dielectric anomaly at T_s (240 K) can be attributed to the variation in the degree of the FeO_5 unit tilting as a presage of the displacive $P6_3mc$–$P6_3cm$ transition at T_{c2}.

■ ASSOCIATED CONTENT

Supporting Information

Experimental details, XRD data, XANES spectra, pyroelectric current, Born effective charge, computed tilting angle of FeO_5 bipyramid unit, and computed ELF contours. This material is available free of charge via the Internet at http://pubs.acs.org.

■ AUTHOR INFORMATION

Corresponding Author

hmjang@postech.ac.kr

Author Contributions

‡These authors contributed equally.

■ ACKNOWLEDGMENTS

This work was supported by the Brain Korea 21 project 2011 and by the World Class University program through the National Research Foundation funded by the Ministry of Education, Science and Technology of Korea (Grant R31-2008-000-10059-0). Computational resources provided by KISTI Supercomputing Centre (Project No. KSC-2011-C1-03) of Korea are gratefully acknowledged.

■ REFERENCES

(1) Wang, J.; Neaton, J. B.; Zheng, H.; Nagarajan, V.; Ogale, S. B.; Liu, B.; Viehland, D.; Vaithyanathan, V.; Schlom, D. G.; Waghmare, U. V.; Spaldin, N. A.; Rabe, K. M.; Wuttig, M.; Ramesh, R. *Science* **2003**, *299*, 1719.

(2) Kimura, T.; Goto, T.; Shintani, H.; Ishizaka, K.; Arima, T.; Tokura, Y. *Nature* **2003**, *426*, 55.

(3) Hur, N.; Park, S.; Sharma, P. A.; Ahn, J. S.; Guha, S.; Cheong, S.-W. *Nature* **2004**, *429*, 392.

(4) Lottermoser, T.; Lonkai, T.; Amann, U.; Hohlwein, D.; Ihringer, J.; Fiebig, M. *Nature* **2004**, *430*, 541.

(5) Spaldin, N. A.; Fiebig, M. *Science* **2005**, *309*, 391.

(6) Katsura, H.; Nagaosa, N.; Balatsky, A. V. *Phys. Rev. Lett.* **2005**, *95*, No. 057205.

(7) Eerenstein, W.; Mathur, N. D.; Scott, J. F. *Nature* **2006**, *442*, 759.

(8) Belik, A. A.; Furubayashi, T.; Matsushita, Y.; Tanaka, M.; Hishita, S.; Takayama-Muromachi, E. *Angew. Chem., Int. Ed.* **2009**, *48*, 6117–6120.

(9) Cheong, S.-W.; Mostovoy, M. *Nat. Mater.* **2007**, *6*, 13.

(10) Choi, T.; Horibe, Y.; Yi, H. T.; Choi, Y. J.; Wu, W.; Cheong, S.-W. *Nat. Mater.* **2010**, *9*, 253.

(11) Ren, C.-Y. *Phys. Rev. B* **2009**, *79*, 125113.

(12) Van Aken, B. B.; Palstra, T. T. M.; Filippetti, A.; Spaldin, N. A. *Nat. Mater.* **2004**, *3*, 164.

(13) Lueken, H. *Angew. Chem., Int. Ed.* **2008**, *47*, 8562.

(14) Oak, M.-A.; Lee, J.-H.; Jang, H. M.; Goh, J. S.; Choi, H. J.; Scott, J. F. *Phys. Rev. Lett.* **2011**, *106*, No. 047601.

(15) Katsufuji, T.; Masaki, M.; Machida, A.; Moritomo, M.; Kato, K.; Nishibori, E.; Takata, M.; Sakata, M.; Ohoyama, K.; Kitazawa, K.; Takagi, H. *Phys. Rev. B* **2002**, *66*, 134434.

(16) Fabrèges, X.; Petit, S.; Mirebeau, I.; Pailhès, S.; Pinsard, L.; Forget, A.; Fernandez-Diaz, M. T.; Porcher, F. *Phys. Rev. Lett.* **2009**, *103*, 067204.

(17) White, R. L. *J. Appl. Phys.* **1969**, *40*, 1061.

(18) Marezio, M.; Remeika, J. P.; Dernier, P. D. *Acta Crystallogr. B* **1969**, *26*, 2008.

(19) Lee, J.-H.; Jeong, Y. K.; Park, J. H.; Oak, M.-A.; Jang, H. M.; Son, J. Y.; Scott, J. F. *Phys. Rev. Lett.* **2011**, *107*, 117201.

(20) Bossak, A. A.; Graboy, I. E.; Gorbenko, O. Yu.; Kaul, A. R.; Kartavtseva, M. S.; Svetchnikov, V. L.; Zandbergen, H. W *Chem. Mater.* **2004**, *16*, 1751.

(21) Lonkai, Th.; Tomuta, D. G.; Amann, U.; Ihringer, J.; Hendrikx, R. W. A.; Többens, D. M.; Mydosh, J. A. *Phys. Rev. B* **2004**, *69*, 134108.

(22) Fennie, C.; Rabe, K. M. *Phys. Rev. B* **2005**, *72*, 100103.

(23) Bulou, A.; Rousseau, M.; Nouet, J. *Key Engr. Mater* **1992**, *68*, 133.

(24) King-Smith, R. D.; Vanderbilt, D. *Phys. Rev. B* **1993**, *47*, 1651.

(25) Stroppa, A.; Marsman, M.; Kresse, G.; Picozzi, S. *New J. Phys.* **2010**, *12*, 093026.